

# Effective Carrier Lifetime in Ultrashort Pulse Laser Hyperdoped Silicon: Sulfur Concentration Dependence and Practical Limitations

Sören Schäfer,\* Xiaolong Liu, Patrick Mc Kearney, Simon Paulus, Behrad Radfar, Ville Vähänissi, Hele Savin, and Stefan Kontermann

Charge carrier lifetime is a crucial material parameter in optoelectronic devices and knowing the dominant recombination channels points the way for improvements. The effective carrier lifetime  $au_{ ext{eff}}$  of surface-passivated hyperdoped (hSi) and nonhyperdoped "black" (bSi) silicon by quasi-steady-state photoconductance decay (QSSPC) measurements and its evolution upon controlled wetchemical etching are studied. Sample preparation involves the irradiation of Si by numerous ultrashort laser pulses either in SF<sub>6</sub> for hSi or ambient atmosphere for bSi. Findings suggest that the hSi is composed of a double layer: 1) an amorphous resolidified top layer with about 92% of the total incorporated sulfur that accounts for the sub-bandgap absorptance and 2) a crystalline layer underneath in which sulfur concentration tails off toward the Si substrate. The effective lifetime is deconstructed by a 1D simulation to quantify the impact of the local lifetime of the defect-rich top layer,  $au_{top}$ . It is found that by the QSSPC method, a maximum  $au_{\mathrm{top}}$  for 1) can be estimated. For 2),  $au_{\mathrm{top}}$  between 2 and 8 ns is estimated. The bSi sample shows a faster lifetime recovery upon etching which suggests that in hSi samples purely laser-induced defects are not limiting the carrier lifetime compared to sulfur-related defects.

# 1. Introduction

Hyperdoping of semiconductors can be used to shift the optical bandgap toward lower energies and thereby extend the optical response of a material like Si further into the infrared.

S. Schäfer, P. Mc Kearney, S. Paulus, S. Kontermann Institute for Microtechnologies (IMtech) University of Applied Sciences RheinMain Am Brückweg 26, DE-65428 Rüsselsheim, Germany E-mail: soeren.schaefer@hs-rm.de

X. Liu, B. Radfar, V. Vähänissi, H. Savin Department of Electronics and Nanoengineering Aalto University Tietotie 3, FI-02150 Espoo, Finland

The ORCID identification number(s) for the author(s) of this article can be found under https://doi.org/10.1002/pssa.202400132.

© 2024 The Authors. physica status solidi (a) applications and materials science published by Wiley-VCH GmbH. This is an open access article under the terms of the Creative Commons Attribution License, which permits use, distribution and reproduction in any medium, provided the original work is properly cited.

DOI: 10.1002/pssa.202400132

Therefore, the approach is attractive for optoelectronic applications, for example, silicon-based infrared photodiodes or intermediate band solar cells.[1-3] A typical hyperdoping method is to combine ion implantation and subsequent pulsed laser melting for recrystallization with dopants like transition metals [Ti, V, Co, Ag, Au], chalcogens [S, Se, Te], and others [N, Mg].<sup>[1]</sup> Here, we realize sulfur hyperdoping by irradiating Si with numerous ultrashort laser pulses in SF<sub>6</sub> atmosphere. An important figure of merit for photodetectors is the ratio  $\tau/t_{\text{transit}}$  of carrier lifetime over transit time through the device or, in this case, the hyperdoped layer and should ideally be as large as possible.<sup>[4–6]</sup> The challenge with hyperdoped materials is that the high concentration of the deep-level impurity states required for sub-bandgap absorptance, however, results in an elevated recombination rate which poses a severe challenge when aiming for a high carrier collection efficiency. An additional source

of defects is the laser process which involves rapid melting/resolidification cycles. It causes high stresses in the substrate and gives rise to crystal defects like dislocations, pressure-induced phase changes, or even void formation.<sup>[7–11]</sup>

A typical characterization method for quantifying the impact of hyperdoping on the recombination rate is to study and measure the effective carrier lifetime  $\tau_{\rm eff}$ , that is, the time (photo-) generated or injected charge carriers prevail in the material system before they recombine. The term "effective" refers to the fact that carriers recombine at different positions, for example, in the bulk or at the surface, or by different mechanisms, for example, by radiative, Auger, or defect recombination (described by Shockley–Read–Hall formalism<sup>[12,13]</sup>), and that  $\tau_{\rm eff}$  is the aggregate of all. This implies that  $\tau_{\rm eff}$  in general depends on the injection level. The generation position within the sample, that is, the excitation wavelength in case of an optical pump, determines the time it takes carriers to reach the recombinative surface layer and thus plays a role as well. Hence,  $au_{\rm eff}$  is only an indirect measure of the local lifetime, for example, within a thin defect-rich surface layer. Previous lifetime studies on hyperdoped Si involved different contactless techniques like optical pump and probing by terahertz pulses, [5] by microwave reflectivity<sup>[15]</sup> or by inductive coupling to the quasi-steady-state photoconductance (QSSPC). Indirect methods like photocarrier transport measure the mobility-lifetime product and require the deposition of Ohmic contacts. The QSSPC method, which we also apply in our study, is widely used in lifetime spectroscopy of Si and directly accesses  $\tau_{\rm eff}$  for a range of injection levels by applying a flash lamp light source and an integrated photodetector. In [19,20]

Our objectives may be summarized by the following questions. 1) How does the effective carrier lifetime  $\tau_{\rm eff}$  relate to the sulfur and laser-induced defect concentration? 2) Is it possible to relate  $\tau_{\rm eff}$  to the local lifetime in the hyperdoped layer? 3) What are the (dis-)advantages of the used lifetime characterization method with respect to its sensitivity in resolving changes of recombination in the hyperdoped layer? 4) What implications can be drawn from a device implementation perspective?

For question 1), we prepare sulfur hyperdoped samples that have been laser processed in SF<sub>6</sub> as well as nominally nonhyperdoped samples laser processed in ambient atmosphere with otherwise identical parameters (pulse density and laser fluence). The latter shall serve as benchmark for laser-induced defects, whereas the hyperdoped samples come with both recombination channels. We then etch the samples for different durations  $t_{\text{etch}}$  in a diluted isotropic Si etch bath at room temperature to successively remove the defect-rich surface layers "top-down". This gives us a set of samples with different concentrations of sulfur and laser-induced defects. After cleaning and surface passivation, we characterize the set of samples by measuring the effective carrier lifetime by the QSSPC method. Furthermore, we determine the absorptance and, for specific samples, the sulfur concentration depth profile by dynamic secondary-ion mass spectrometry (SIMS). In addition, we examine the surface morphology by scanning electron microscopy (SEM).

For question 2), we conduct a simplified 1D numerical modelling where we vary the local lifetime of the hyperdoped top layer and study its impact on  $\tau_{\rm eff}$ . This helps to identify the sensitivity of the lifetime characterization method with respect to the recombination rate within the hyperdoped silicon (hSi) which addresses question 3) as well as the effect of the electrically active dopant concentration within the hSi. For question 4) we discuss what our findings could imply for device implementation.

# 2. Results

Figure 1 shows SEM micrographs of the tilted cross section of the hSi samples after different etch durations. The upper-left micrograph illustrates the "as-processed" sample surface without explicit back etching. The randomly arranged cone structures have a height between 3 and 5 µm. Their surface appears rather fuzzy due to a nanometer-sized subtexture. From transmission electron microscopy (TEM) analysis on similar structures, it is known that the cones typically have a resolidified surface layer which contains amorphous, nano-, and polycrystalline phases as well as voids. After  $t_{\text{etch}} = 60 \text{ s}$ , the surface of the cones has eroded and appears rougher on a nanometer scale, but the original cones are still visible. After 300 s, the outline of the original cones vanished as their tips were mostly etched off. The morphology of the nanometer-sized erosions that were formed before transferred to an overall rough surface. However, the surface is rather smooth but fuzzy. For yet longer etch durations, the surface morphology becomes more planar, as we would expect from an isotropic etch.

**Figure 2**a shows the absorptance spectra of the *hSi* samples up to  $t_{\rm etch} = 600$  sec as well as for the nonetched *bSi* sample and a polished crystalline silicon wafer (*cSi*). Up to a wavelength of about 1 μm, the nonabsorbed photons are due to external surface reflection. This fraction is reduced for both *bSi* and *hSi* over the *cSi* reference due to the microstructured surface morphology. At a wavelength of 600 nm, the absorptance of *hSi* first increases with  $t_{\rm etch}$  up to 94%<sub>abs</sub> for  $t_{\rm etch} = 30$  s and then decreases again to 83%<sub>abs</sub> for  $t_{\rm etch} = 600$  s. The average sub-bandgap absorptance  $\overline{A}_{1250-2500}$  for wavelengths  $\lambda > 1250$  nm and up to the detection limit ( $\lambda = 2500$  nm) of the spectrophotometer remain nearly constant for the *hSi* and decrease monotonously with  $t_{\rm etch}$  from (65.5 ± 1.9) %<sub>abs</sub> for the nonetched sample (0 s) to (0 ± 1.2) %<sub>abs</sub> after 300 s (see **Figure 3**a). The *bSi* sample shows sub-bandgap absorptance as well which, however, decreases with wavelength.

Figure 2b shows the sulfur concentration profiles obtained by SIMS for specific hSi samples with different  $t_{\rm etch}$  and for the non-etched bSi. The sulfur concentration decreases with  $t_{\rm etch}$  for hSi as expected and is lowest for the bSi sample. The shown depths are calculated from the respective sputter time and the calibration factor obtained from measuring the crater depth

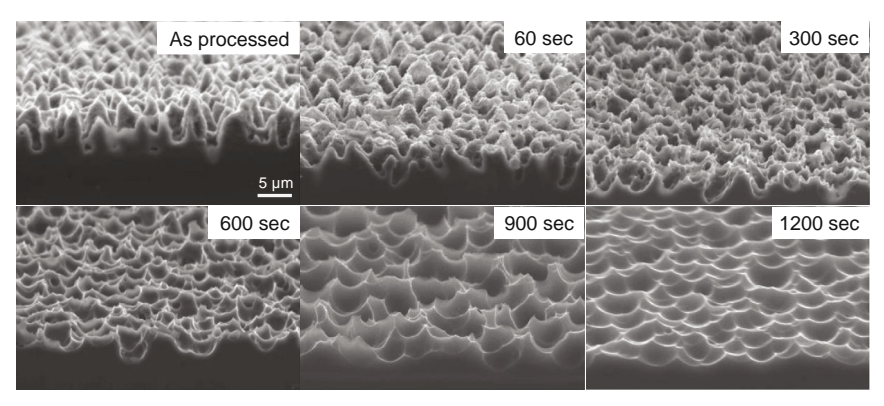


**Figure 1.** SEM micrographs of the tilted cross section of hSi samples etched for the stated duration. Defect-rich, amorphous, and polycrystalline regions with high sulfur content are preferentially etched. After about 300 s, the isotropic etch polishes the surface. The scale bar is the same for each micrograph.

www.advancedsciencenews.com



www pss-a com

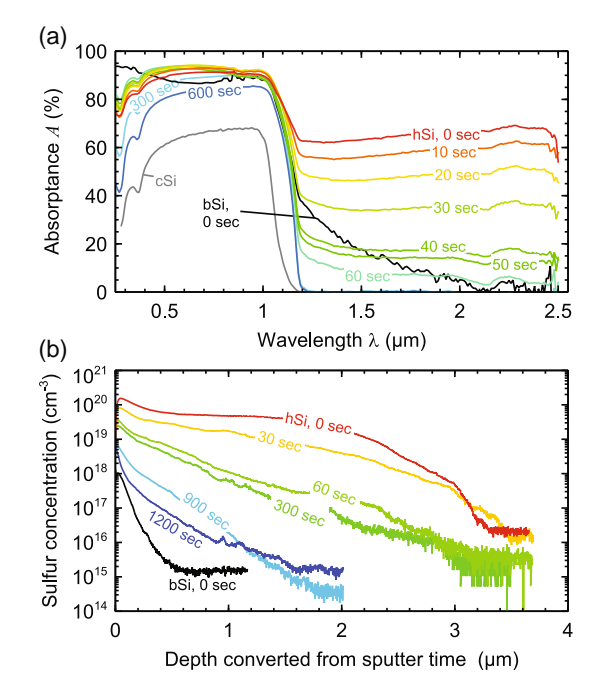


Figure 2. a) Absorptance spectra and b) SIMS profiles of hSi samples laser processed in SF $_6$  and etched for different durations  $t_{
m etch}$ . Black curves refer to the nonetched bSi sample processed in atmosphere.

on the planar calibration standard. The profile of the nonetched hSi peaks at a sulfur concentration of  $(1.5 \pm 0.1) \times 10^{20}$  cm<sup>-3</sup> at  $(40 \pm 3)$  nm, then decreases to  $(5.1 \pm 0.1) \times 10^{19} \, \text{cm}^{-3}$  at  $(0.75 \pm 0.06)~\mu m$ , and shows a plateau until  $(1.85 \pm 0.1)~\mu m$  with a concentration of  $(2.5 \pm 0.1) \times 10^{19}$  cm<sup>-3</sup>. This is also the maximum concentration obtained for the  $t_{\rm etch} = 300~{\rm s}$  sample. Beyond this depth, concentration declines to the detection limit at about 3.3 µm. The rough surface morphology, which above all varies with  $t_{\text{etch}}$ , and inhomogeneous material composition add uncertainty to the depth resolution, which will be discussed below. SEM cross-section micrographs of the sputter crater of the nonetched hSi (see Figure S2, Supporting Information) point to a nonconformal sputter rate as the cone structures basically disappear. The hSi sample with the largest etch duration exhibits a higher sulfur concentration than the nonetched bSi sample. The small yet significant sulfur signal of the latter could be due to matrix effects or mass interference with oxygen species.<sup>[22]</sup>

Figure 3a,b shows the average sub-bandgap absorptance and the sulfur dose obtained from integrating the sulfur profiles over the depth versus  $t_{\text{etch}}$  for hSi and bSi, respectively. Within the first minute of etching ( $t_{\text{etch}} \leq 60 \text{ s}$ ), the average sub-bandgap absorptance drops from (65.5  $\pm$  1.9)  $\%_{abs}$  to (6.8  $\pm$  1.9)  $\%_{abs}$  and the sulfur dose from  $(11.4 \pm 1.7) \times 10^{15}$  to  $(0.9 \pm 0.1) \times 10^{15}$  cm<sup>-2</sup>. This indicates that 92%<sub>rel</sub> of the incorporated sulfur are within the first 150-200 nm if we take the etch rate of the solution on crystalline Si for granted. After the sub-bandgap absorptance vanished at  $t_{\text{etch}} = 300 \text{ s}$ , the sample has a remaining sulfur dose of (0.59  $\pm$  0.08)  $\times\,10^{15}\,\text{cm}^{-2}.$ 

Figure 3c,d show the measured effective carrier lifetimes as obtained by QSSPC and spatially resolved as obtained by PL imaging, respectively. The PL images show the non-laser

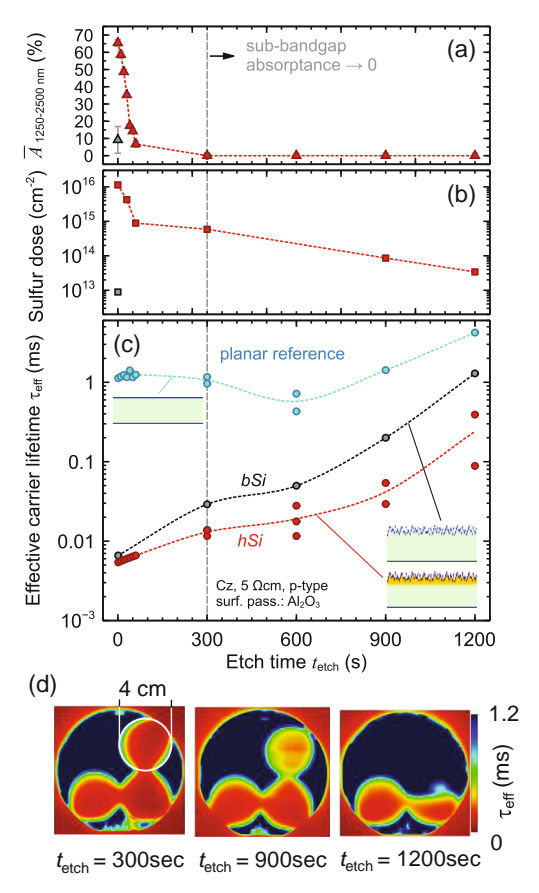


Figure 3. a) Average sub-bandgap absorptance in the spectral range between 1250 and 2500 nm, b) sulfur dose, and c) effective minority carrier lifetime  $\tau_{\rm eff}$  at an injection level of  $\Delta n = 10^{15} \, {\rm cm}^{-3}$  for hyperdoped samples (red symbols) versus etch duration. Gray symbols refer to the case of a,b) nonetched reference sample laser processed in atmosphere and the (c) turquoise symbols mark  $\tau_{\rm eff}$  of the non-laser processed reference area. Dashed lines in (c) are guide to the eye through the average values. The vertical dashed line marks the first observation of vanished sub-bandgap absorptance, here after  $t_{\rm etch} = 300$  s. The insets in (c) show sketches of the cross sections of planar, black, and hyperdoped samples, the latter with a rough and sulfur-rich front surface (yellow), and Al<sub>2</sub>O<sub>3</sub> passivation on both sides (blue). d) Scaled PL images of wafers after three different etch durations. The upper-left area is non-laser processed, the upper-right circular area is laser processed in atmosphere, and the two lower areas are nominally identical laser processed in SF<sub>6</sub>.

processed and planar reference area in the upper-left region, the circular bSi area in the upper right, and the two circular hSi areas in the lower row for different  $t_{\rm etch}$ . The effective carrier lifetime  $\tau_{\rm eff}$  of the planar reference is essentially independent from  $t_{\text{etch}}$  with lifetimes between 1 and 1.5 ms, with a low  $(575 \pm 135)$  µs outlier at  $t_{\rm etch} = 600 \, \rm s$  and a high  $(4200 \pm 300)$  $\mu$ s outlier at  $t_{\text{etch}} = 1200 \text{ s}$ . The separation of the contributions from bulk and surface recombination via the Kane and Swanson method<sup>[23]</sup> yields that the outliers are mainly due to different bulk qualities, as the low (high) outlier does not coincide with the highest (lowest) surface recombination rate. The nonetched bSi (black symbols) and hSi (red symbols) samples have low  $\tau_{\rm eff}$  values of (6.6  $\pm$  0.3)  $\mu s$  and (5.4  $\pm$  0.2)  $\mu s$ , respectively.



Within the first 60 s of etching hSi, that is, after the removal of the sulfur-rich layer,  $\tau_{\rm eff}$  rises monotonously with  $t_{\rm etch}$  by 18%<sub>rel</sub> to  $(6.6 \pm 0.3)$  µs for  $t_{\rm etch} = 60$  s. At  $t_{\rm etch} = 300$  s, that is, after the loss of sub-bandgap absorptance,  $au_{
m eff}$  increased to (13  $\pm$  1)  $\mu s$  for hSi and  $(29 \pm 2)$  µs for bSi. It becomes clear that the effective carrier lifetime of bSi recovers faster than for hSi. After the maximum  $t_{\text{etch}}$  applied in our experiment, the  $\tau_{\text{eff}}$ -value for hSi approaches (240  $\pm$  150)  $\mu$ s while the value for bSi takes (1291  $\pm$  100) µs which is essentially the quality of the cSi bulk. The PL images in Figure 3d illustrate that the recovery of the lifetime is not homogeneous across the laser processed area, either due to a spatial variation in etch rate or hyperdoping profile, which explains the larger uncertainty of the values for hSi. However, the general trend shows that while both laser-induced crystal damage and incorporated sulfur severely reduce the effective carrier lifetime  $\tau_{\rm eff}$ , the sulfur states reach deeper into the substrate and set the major limitation in the hSi samples as they result in a higher recombination rate for all investigated etch durations.

# 3. Simulation

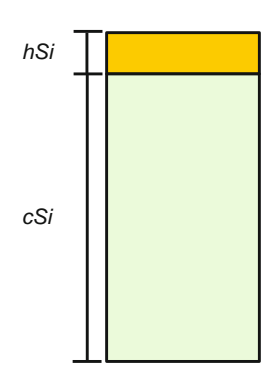
As mentioned above, the effective carrier lifetime  $\tau_{\rm eff}$  comprises all recombination channels present in a sample. In the present case, however, defect recombination in the laser-processed surface layer determines and limits the measured value of  $\tau_{\text{eff}}$  of both bSi and hSi samples. We set up a simulation of the lifetime measurement in the open-source software PC1D that solves the set of Poisson's, transport, and continuity equations for both carrier types in 1D.<sup>[24]</sup> Figure 4 shows a sketch of the simulated geometry together with part of the assumptions and varied parameters. If not mentioned otherwise, the physical properties like bandgap, refractive index, etc. are taken from Si as preset in the software. Carrier mobilities and free carrier absorption are calculated from an internal model. We simulate the effective carrier lifetime by the temporal decay of the excess photoconductivity after an initial photogeneration at time t = 0. Note that this refers to the so-called transient mode with no illumination during data acquisition, whereas the measurements are taken under (quasi-) steady-state mode under a flash with decay constant of about 2 ms. Simulations under steady state, however, yield

similar results. The spectrum of the illumination corresponds to the spectrum of the flash lamp. [25] Its intensity is adapted, depending on the local lifetime in the hyperdoped region  $\tau_{top}$ , to allow for an excess carrier density in the cSi bulk of  $10^{15}\,\mathrm{cm}^{-3}$ , as this is the injection level of the experimental values in Figure 3c. We assume no surface recombination and a bulk lifetime of the substrate of 1 ms based on the measurements of the reference area. Note that the actual bulk lifetime of the material is likely higher, which results in a higher uncertainty of the simulated when bulk recombination cannot be neglected over recombination in the hSi. The absorption coefficient of the hSi layer is adapted, as shown in Figure 4, to account for a higher absorptance of IR photons. Its value is estimated from the analysis in ref. [26] for an assumed optical depth of 0.03 ( $T_{anneal} = 400$  °C) and a thickness of the hyperdoped layer of 1 µm. Thereby, about one-third of the total photogeneration takes place within the hSi. The two parameters bulk lifetime  $\tau_{top}$  and dopant concentration  $N_{\rm D}$  in the hSi layer are varied to study their respective impact on the effective lifetime of the whole sample stack.

Figure 5 shows the dependence of the simulated effective carrier lifetime  $au_{eff}$  on  $au_{top}$  as well as on different n-type dopant concentrations  $N_D$ . The undoped case refers to the same p-type doping of the hSi as the cSi substrate. For all dopant concentrations, there is an interval of  $au_{top}$ -values for which the effective carrier lifetime depends strongly on the local hSi carrier lifetime. If  $\tau_{\rm top}$  exceeds a certain value,  $\tau_{\rm eff}$  approaches the bulk lifetime of the substrate; if it falls below a certain value,  $au_{ ext{eff}}$  takes a lower limit and does not change significantly with  $\tau_{top}$ . The trend with respect to the n-type dopant density is that a higher  $N_D$  results in a higher effective carrier lifetime for a given hSi lifetime  $au_{top}$ . An exception is the lower  $\tau_{\text{eff}}$ -limit for the undoped case, which is  $11\,\mu s$  and thereby higher than the lower limit for an assumed  $N_{\rm D} = 10^{16} \, {\rm cm}^{-3}$  of 5 µs. We find that the measured effective carrier lifetimes in Figure 3c are best modeled by assuming a dopant concentration of  $N_D = 10^{16} \,\mathrm{cm}^{-3}$  or lower and local top layer lifetimes in the range from few ps up to 10 µs.

# 4. Discussion

The hyperdoped layer is composed of 1) a resolidified amorphous, nano-, and polycrystalline top layer that here contains



Parameter	Value
Surface recombination velocity	0 cm/s
Illumination spectrum	flash lamp of WCT-120 [*]
hSi	
Thickness	1 μm
Absorption coefficient $\alpha$	250-660nm: Si literature values; 660-1300nm: $\alpha$ = 300 cm <sup>-1</sup> (fixed)
Bulk lifetime $\tau_{\text{top}}$	Varied between 5 ps to 10 µs
Dopant concentration	Varied between undoped or n-type
cSi	
Thickness	300 μm
Bulk lifetime $\tau_{\text{bulk}}$	1000 μs (fixed)
Dopant concentration	2.78×10 <sup>15</sup> cm <sup>-3</sup> (fixed), p-type

Figure 4. Sketch of the simulation and summary of a part of the assumed and varied sample parameters. The upper and lower layer refer to the hyperdoped (hSi) and crystalline bulk (cSi) silicon. The 2D sketch is for illustration only. \*Flash lamp spectrum from ref. [25].

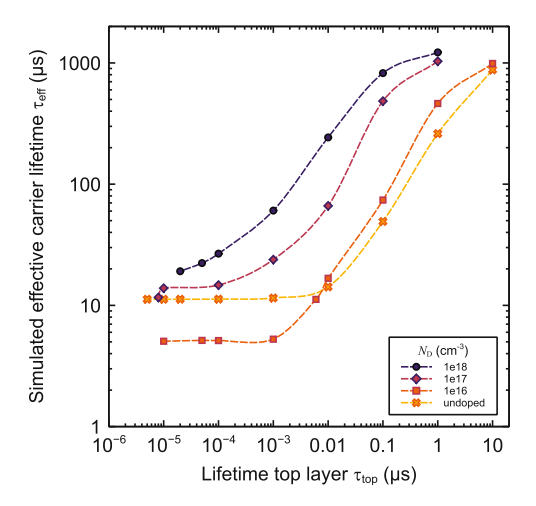


**Figure 5.** Simulated effective carrier lifetime  $\tau_{\rm eff}$  of the sample as shown in Figure 4 versus the assumed lifetime in the top hSi layer for different n-type dopant concentrations  $N_{\rm D}$ . *Undoped* means the hSi layer has the same p-type dopant concentration as the cSi bulk.

92% of the incorporated sulfur dose with a rather uniform distribution of the dopant and 2) a crystalline layer underneath in which the sulfur concentration gradually decreases.<sup>[1]</sup> We deduce from the controlled back-etch experiment that the resolidified top layer has a thickness between 150 ( $t_{\rm etch} = 60 \, {\rm s}$ ) and 750 nm  $(t_{\rm etch} = 300 \text{ s})$ . It also accounts for the sub-bandgap absorptance of the material. The initial increase in absorptance in the visible region for  $t_{\text{etch}} < 30 \,\text{s}$  could be attributable to morphology changes but more likely it is due to a thinning/removal of a thin amorphous top layer that forms nearly conformally on the surface due to the scanning movement of the laser beam across the surface. [9] The higher refractive index of amorphous silicon results in a higher surface reflectance. [27] Figure S1, Supporting Information, shows Raman spectra of the corresponding samples that yield a fully crystalline material after  $t_{\rm etch} = 300 \, \rm s.$ The SEM micrographs indicate that the resolidified, defect-rich, and highly doped layer is preferentially etched, [28,29] so the thickness bounds are likely underestimated. TEM analyses in literature also show thickness inhomogeneities with resolidified material concentrating especially in the tip region of the cone structures where its thickness can exceed 1 µm. [9,21] The SIMS profile of the nonetched sample in Figure 2c shows highest concentration up to a depth of (0.75  $\pm$  0.06)  $\mu m$  and a wider plateau until (1.85  $\pm$  0.1)  $\mu m$  after which concentration gradually decays. We assume that after the first interval, the resolidified layer has been removed in regions of lower thickness between the protrusions and that the plateau arises from sulfur in the tip region. As already mentioned in Section 3, the depth resolution of the SIMS profiles is limited due to an initially nonconformal sputter rate and varying composition of the layers. As the sputter rate depends on the angle of incidence of the ion beam and the morphology changes with the amount of sputtered material, the local rate also changes over acquisition time. [30,31] This dependency on morphology and composition likely explains why the sulfur profile of the  $t_{\text{etch}} = 300 \text{ s}$  sample differs in shape and depth from final decay in sulfur concentration of the nonetched sample.

The profile of the  $t_{\rm etch} = 300$  s sample is stretched in comparison, suggesting a lower sputter rate for this morphology and composition.

For the 1D simulation, we do not distinguish between the two layers and simplify the hSi layer as a 1  $\mu$ m-thick layer of elevated recombination, whereas actually the carrier lifetime depends on the crystal quality<sup>[8]</sup> and the dopant concentration.<sup>[32,33]</sup> Furthermore, the absorption coefficient in the hSi is in practice linked to the local lifetime but kept fixed for all  $\tau_{\rm top}$ . However, the main trends and dependencies are reflected in Figure 5.

The first trend is the dependency on  $\tau_{top}$ . The lower limit where  $au_{ ext{eff}}$  does not depend on  $au_{ ext{top}}$  is due to the diffusion-limited carrier transport from the bulk to the *hSi*. That means that at this level even a higher number of defects does not reflect in a change of  $\tau_{\rm eff}$ . Effective carrier lifetimes of 5 and 11 µs correspond to electron diffusion lengths of 127 and 189 µm, respectively, for the given substrate. This covers the average distance between position of photogeneration and hSi and means instantaneous recombination once the carriers reach the hSi. If we switch the incident illumination to the rear, that is, the non-laser processed side in the simulation, we observe a slightly higher  $\tau_{\rm eff}$  as this avergage distance increases. For a simulated dopant concentration of  $N_D = 10^{16} \,\mathrm{cm}^{-3}$ , the lower limit is reached for  $\tau_{\rm top}$  < 2 ns, that is, measured effective carrier lifetimes of—in this case—5 µs mean carrier lifetimes in the hSi below 2 ns. For dopant concentrations of 10<sup>20</sup> cm<sup>-3</sup>, carrier lifetimes of about 1 ns and diffusion lengths of below 1 µm are reported. [32] This yields that for a  $\tau_{top} > 2$  ns, the diffusion length of carriers exceeds the thickness of the hSi layer. Hence, they may transverse the hSi into the bulk of the substrate, resulting in an increase of  $au_{\rm eff}$ . This increase continues until  $au_{\rm top} > 10\,\mu s$  where the cumulative recombination in the hSi does not limit  $au_{ ext{eff}}$  anymore. At this level, the neglection of surface recombination in the simulation certainly should be reconsidered for more accuracy. Note that the slight but significant increase in  $\tau_{\rm eff}$  for the experimental samples in Figure 3c for  $t_{\text{etch}} \leq 60 \text{ s}$  is not reflected in the simulation. This likely results from the fixed absorption coefficient-and thus also fixed generation profile-in the simulation. In the experiment, a larger fraction of carriers is generated in the cSi bulk when the hSi becomes etched which also influences  $\tau_{\rm eff}$  .<sup>[15]</sup>

The second trend is in the dopant concentration  $N_D$  of the hSi. Two aspects come into play that differ depending on  $N_D$ . The first is that an n-type doping results in a space-charge region at the interface to the substrate. The charge carriers become separated and diffusion of electrons (holes) into the substrate (hSi) reduces due to the energy barrier. The height of the energy barrier increases with dopant concentration and furthermore depends on the injection level and thereby also on the local carrier lifetime  $\tau_{\text{top}}$ . It "screens" the recombinative hSi from the cSi bulk by reducing the replenishing flow of recombination partners. The undoped case without any space-charge region therefore shows the lowest  $\tau_{\rm eff}$  values. The exception for  $N_{\rm D}=10^{16}\,{\rm cm}^{-3}$  for  $\tau_{\rm top}$  < 2 ns is due to a high recombination rate at the hSi/cSi interface. The reason is due to the second aspect, which is that recombination rate is proportional to the product of electron n and hole density p. The electric field drives a drift current of electrons from the cSi toward the hSi that quickly replenishes recombined carriers, thus resulting in a higher p-n product and an overall

faster decay compared to the undoped case at the interface. However, if  $N_{\rm D}$  becomes larger, the countereffect of holes drifting into the cSi combined with a higher-energy barrier becomes important. Figure S3, Supporting Information, shows more details on spatially resolved recombination and carrier densities.

It might seem contradictory that the experimental values are best matched by a simulated  $N_{\rm D}=10^{16}\,{\rm cm^{-3}}$  although the sulfur concentration is above  $10^{19}\,{\rm cm^{-3}}$ . Even if only 1–10% of the sulfur is electrically active as donor, [11,34–36] there is a large discrepancy. The reason is that the crystalline tail region limits  $\tau_{\rm eff}$  of the sample and the effective doping here is much lower than in the resolidified layer. **Figure 6**a shows a replot of the measured  $\tau_{\rm eff}$  values of hSi samples over the sulfur dose calculated from the SIMS profiles. In the process of thinning and removal of the resolidified layer, although it contains most of the sulfur and crystal defects,  $\tau_{\rm eff}$  changes insignificantly. Only after its removal and the onset of thinning the underlying sulfur-containing crystalline silicon,  $\tau_{\rm eff}$  increases significantly. This suggests that the used conditions of measuring and studying the effective lifetime are especially sensitive to the tail region and hold limited insight with respect to the resolidified layer.

For the same etch duration, the lifetime of the bSi shows a stronger recovery. The sample shows a microstructured cone-like morphology as well. Its sub-bandgap absorptance is due to Urbach states that result from amorphous and polycrystalline phases and small amounts of incorporated oxygen and nitrogen. Previous studies suggest that incorporation of nitrogen from  $N_2$  is less efficient than from, for example,  $NF_3$  precursor gas. We therefore assume a similar two-layer composition as for the hSi, with the main difference that bSi is essentially free of sulfur. The resolidified layer becomes removed in a similar duration as for the hSi so we can infer a benchmark for the recombination due to laser-induced defects

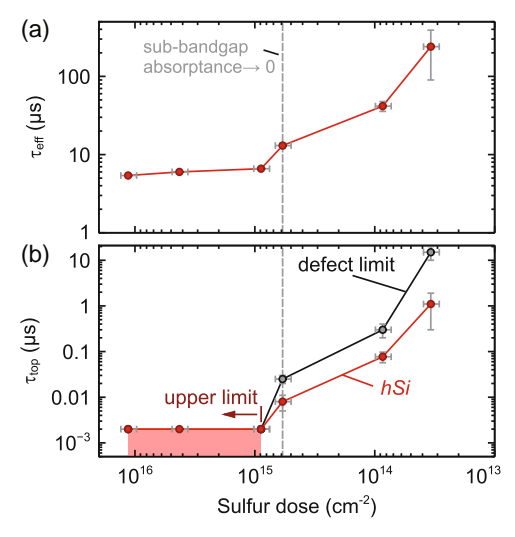


**Figure 6.** a) Measured effective carrier lifetime  $\tau_{\rm eff}$  of the hSi sample as shown in Figure 3c versus the sulfur dose obtained by SIMS measurements. b) Corresponding local hSi bulk lifetime  $\tau_{\rm top}$  obtained from correlating the measured  $\tau_{\rm eff}$  to the simulated  $\tau_{\rm eff}$  in Figure 5 for  $N_{\rm D}=10^{16}\,{\rm cm}^{-3}$ . The upper limit for three highest sulfur doses is  $\tau_{\rm top}<2$  ns. We estimate the "defect limit" due to laser-induced damage from the bSi sample.

from the bSi. Figure 6b shows the local lifetime  $\tau_{top}$  that we obtain from Figure 5 by correlating the measured (Figure 3c) and simulated  $\tau_{\rm eff}$  for hSi (red) and bSi (black) versus sulfur dose. For bSi, we take the curve of the undoped, for hSi the  $N_{\rm D} = 10^{16} \, {\rm cm}^{-3}$  curve for the for shorter and undoped for the two longest  $t_{\text{etch}}$  for correlation. The uncertainties in the measured  $\tau_{\rm eff}$  values and due to the choice of  $N_{\rm D}$  are reflected by the vertical error bars. As mentioned, we interpret the values for  $\tau_{\text{top}}$  from bSi with the same  $t_{\text{etch}}$  as the "defect limit," that is, the lifetime in the crystalline tail region if no sulfur and only laser-induced defects were present. After the longest  $t_{\text{etch}} = 1200$ s, this limit yields a  $\tau_{top}$ -value of at least 10 µs, which means that we cannot ensure that all defects have been removed but only that they do not limit  $\tau_{\rm eff}$  anymore. We estimate the etch depth at this point to be at least 3 µm. Liu et al. report a full lifetime recovery at an etch depth of 9 µm in a similar back-etch experiment, but most of the defects are already removed at a depth of 4.5 µm. [20] We find that the crystalline tail region in the hSi has a local carrier lifetime  $\tau_{top}$  between 2 and 8 ns after the removal of the resolidified layer whereas the defect limit after the same etch duration holds a  $\tau_{\text{top}}$  of about 25 ns. For higher doses where the resolidified layer is still present, we can only infer an upper limit of  $\tau_{\text{top}}$  < 2 ns. Lifetime characterization methods with higher temporal resolution and monochromatic excitation in the hyperdoped layer itself report values of the resolidified layer between 1 and 200 ps, depending on dopant concentration.<sup>[5]</sup>

#### 5. Conclusion

We produce hyperdoped (hSi) and nonhyperdoped (bSi) silicon by ultrashort laser pulse irradiation in SF<sub>6</sub> and ambient atmosphere, respectively. The laser process creates a surface texture of randomly arranged micrometer-sized cones. A controlled wet chemical back etch procedure leads to a set of samples with a variety of sulfur concentrations. Based on our characterization, we can distinguish two different layers that compose the hyperdoped surface: 1) a resolidified amorphous, nano-, and polycrystalline top layer that contains about 92% of the incorporated sulfur in a rather uniform distribution and that makes up for the sub-bandgap absorptance and 2) a crystalline layer with a declining sulfur concentration. We estimate the thickness of the resolidified top layer between 150 nm in its thinnest extension between the cones and (1.85  $\pm$  0.1)  $\mu m$  within the cone tips. The thickness of the underlying layer is inhomogeneous as well but based on the SIMS profile it should lie in a similar range.

The examination of the effective carrier lifetime of the sample set yields the following conclusions based on the questions we raised in the introduction. 1) How does the effective carrier lifetime  $\tau_{\rm eff}$  relate to the sulfur and laser-induced defect concentration? We take the bSi sample as a benchmark for laser-induced defects that we assume has a similar double layer composition as the hSi. The finding of a faster recovery of  $\tau_{\rm eff}$  of bSi over hSi during "top down" wet chemical etching suggests that on the one hand, laser-induced defects do not reach as deep into the substrate as the sulfur and, on the other hand, that within the hSi, it is the sulfur and not the laser-induced crystal damage that mainly limits  $\tau_{\rm eff}$ . A significant increase in  $\tau_{\rm eff}$  is only observed after the removal of the resolidified layer. This suggests



www.advancedsciencenews.com



that the measured  $au_{
m eff}$  refers to the diffusion-limited lifetime as long as the resolidified layer is present and that carriers recombine "instantaneously" once they reach this layer, at least for the temporal resolution of the used setup. 2) Is it possible to relate  $\tau_{\rm eff}$  to the local lifetime in the hyperdoped layer? We estimate the local lifetime  $\tau_{\text{top}}$  in the defect-rich hSi by comparing the measured  $\tau_{\rm eff}$  with the ones obtained from a 1D simulation with simplifying but justified assumptions for different  $\tau_{\text{top}}$ . We find that the highly recombinative resolidified layer has a maximum  $\tau_{top}$  of 2 ns. The crystalline layer with the declining sulfur concentration has  $\tau_{\text{top}}$  between 2 and 8 ns and the sulfur-free bSi sample with the same etch duration a  $\tau_{\text{top}}$  of about 25 ns. If  $\tau_{\text{top}}$  approaches a value of at least 10 µs,  $\tau_{\rm eff}$  is not limited by recombination in hSi anymore. 3) What are the (dis-)advantages of the used lifetime characterization method with respect to its sensitivity in resolving changes of recombination in the hyperdoped layer? The QSSPC method as implemented in the setup has the advantage that in principle it gives the injection dependence of  $\tau_{\rm eff}$  in a quick and easy-to-apply procedure. A challenge is linked to the spectrum of the flash lamp that generates charge carriers in the hSi as well as in the cSi bulk. As for hSi samples,  $\tau_{\rm eff}$  is determined by the time it takes carriers to diffuse from cSi to the hSi, the measured  $\tau_{\rm eff}$  varies with, for example, the excitation wavelength, the absorption coefficient of the hSi, or whether we illuminate from the front or rear side. The lifetime within the resolidified layer remains obscured. An interesting feature is that the doping of the tail region influences  $\tau_{\rm eff}$  as it can "screen" carriers from the resolidified layer. By our measurements, we estimate that the effective n-type doping concentration of this region is of the order 10<sup>16</sup> cm<sup>-3</sup>. Thus, the QSSPC method in principal yields information of the electrically active dopant density of the hSi tail region. For detailed information of the local lifetime in the resolidified layer, exclusive photogeneration within this layer as well as a higher temporal resolution of the lifetime measurement are necessary. 4) What implications can be drawn from a device implementation perspective? The controlled back etching of the resolidified layer could prove beneficial for the performance of the material as an IR photodetector device as it tunes the figure of merit  $\tau/t_{\text{transit}}$ . Wang et al. showed improvement in responsivity at least at an above-wavelength illumination of 1064 nm of a similar material after reactive ion etching.<sup>[43]</sup> There may be an optimum trade-off between the positive effects of an elevated local carrier lifetime  $\tau$  on a scale below the "detection limit" of 2 ns, a possible increase of carrier mobility, lower layer thickness which both affect transit time, and the negative effects of reduced sub-bandgap absorptance. For an estimate on the figure of merit, however, carrier mobility and electrical active sulfur concentration for determining the built-in voltage should be characterized in addition to the parameters obtained in our study.

# 6. Experimental Section

Sample Preparation: We used double-side polished, Czochralski-grown crystalline silicon (cSi) wafers with a diameter of 4", a (100)-crystal orientation, p-type resistivity of 1–10  $\Omega$ cm, and a thickness of (380  $\pm$  10)  $\mu$ m. For sulfur hyperdoping, we placed the wafer into a cylindrical vacuum chamber which we filled by sulfur hexafluoride (SF<sub>6</sub>) to a pressure of 675 mbar according to the procedure described in ref. [44]. For laser

processing in atmosphere, we placed the wafers on the chamber chuck without the cover and used a laser fume suction to reduce dust and debris. The Yb:YAG laser system (Amplitude Tangor 100) emitted pulses at the central wavelength 1030 nm with 10 ps pulse duration at a repetition rate of 200 kHz. A two-axis galvanometer scanner with an f-theta lens (focal length 340 mm,  $1/e^2$ -beam diameter of 70 µm) scanned the pulses across the wafer in a square-shaped grid pattern with a scanning speed of 555 mm s<sup>-1</sup> (spot-to-spot distance  $\Delta x = \Delta y \approx 2.8 \,\mu\text{m}$ ). This resulted in a total number of pulses per spot of N = 500. The peak fluence was  $\phi_0 = 1.4 \,\mathrm{J\,cm^{-2}}$ . The circular laser processed areas had a diameter of 4 cm. Most wafers designated for back etching came with one area processed in atmosphere and two nominally identical areas processed in SF<sub>6</sub>. We used the sequence of first processing the area in atmosphere and then in SF<sub>6</sub> to avoid any possible cross contamination by sulfur-containing debris. Due to the induced surface structure, both laser-processed areas appeared almost black but since the latter was additionally hyperdoped by sulfur, we termed the former "bSi" and the latter "hSi." Part of the wafers only came with three identical hSi areas. We additionally produced a bSi sample with areas processed in atmosphere only for absorptance and secondary-ion mass spectrometry (SIMS) measurement as reference.

After laser processing the samples were precleaned by rinsing in a sequence of acetone, isopropanol, and deionized (DI) water. A 2 min dip in hydrofluoric acid (HF) removes any oxide layer. We then applied an isotropic Si etch consisting of HF (50 wt%), nitric acid HNO<sub>3</sub> (70 wt%), and DI water in a mixing ratio of 1:20:29 in a total volume of 2.5 L. We estimated the etch rate of this solution on planar cSi to be (150  $\pm$  25) nm min $^{-1}$ . We applied etch durations  $t_{\rm etch}$  of 10, 20, ..., 60, 300, 600, 900, and 1200 sec on separate wafers. We then applied a standard clean (SC1 and SC2) including HF dip. Subsequently, both front and rear surfaces were passivated by 50 nm atomic layer deposited Al<sub>2</sub>O<sub>3</sub> (dep. temperature 200 °C, precursors trimethylaluminium and H<sub>2</sub>O as in another study  $^{[45]}$ ) and annealed at 400 °C (30 min, forming gas ambient) to activate the passivation.

Characterization: We first measured the effective carrier lifetime  $\tau_{\rm eff}$  by QSSPC decay (Sinton WCT-120). We placed the center of each laserprocessed area over the center of the coil of the setup that detected the photoconductance. This coil was calibrated for samples with a diameter of 4 cm. We illuminated the samples from the laser-processed side and evaluated  $\tau_{\rm eff}$  at an excess minority carrier density of  $\Delta n = 10^{15} \ {\rm cm}^{-3}$ . The optical constant during measurement was kept fixed at 0.7 for planar samples and 0.9 for laser-processed samples. Changes in morphology due to etching were not accounted for as the impact of the constant on  $au_{\rm eff}$  was below 10%<sub>rel</sub>. We additionally performed photoluminescence (PL) imaging (BTI LIS-R2 PLUS) for spatial resolution of  $\tau_{\rm eff}$ . We then removed the surface passivation layer again by HF dip (1 wt% for 5 min) and cleaved the samples for scanning electron microscopy characterization. Absorptance is measured by a spectrophotometer by placing the samples in an integrating sphere according to the method described in another study. [26] We measured sulfur depth profiles by dynamic SIMS Cameca IMS 4f-E6 of specific samples without additional HF dip prior to measuring. The system was calibrated by a planar S/Si implantation standard. Data acquisition and thus sputtering time terminated when the background signal was reached. The measurement area was (120  $\times$  120)  $\mu$ m<sup>2</sup>.

# **Supporting Information**

Supporting Information is available from the Wiley Online Library or from the author.

# Acknowledgements

This work was funded by the Federal Ministry of Education and Research of Germany under grant no. FKZ 03INT701AA and by Business Finland through the "FemtoBlack" project under grant no. 7479/31/2019. S.S. acknowledges funding by the German Federal Ministry of Education and Research in the context of the federal-state program "FH-Personal"



#### www.advancedsciencenews.com



under the grant number 03FHP147A (REQUAS). X.L. acknowledges financial support of the Research Council of Finland (#354199). B.R. and V.V. acknowledge financial support of the Research Council of Finland (#331313). The work is related to the Flagship on Photonics Research and Innovation "PREIN" funded by Research Council of Finland. Part of the research was performed at the Micronova Nanofabrication Centre of Aalto University.

Open Access funding enabled and organized by Projekt DEAL.

#### **Conflict of Interest**

The authors declare no conflict of interest.

# **Data Availability Statement**

The data that support the findings of this study are available from the corresponding author upon reasonable request.

# **Keywords**

effective carrier lifetime, hyperdoping, silicon, simulation, wet-chemical etching

Received: January 31, 2024 Revised: April 15, 2024 Published online: May 2, 2024

- [1] M.-J. Sher, E. G. Hemme, Semicond. Sci. Technol. 2023, 38, 33001.
- [2] Z. Tong, M. Bu, Y. Zhang, D. Yang, X. Pi, J. Semicond. 2022, 43, 93101.
- [3] A. Luque, A. Martí, C. Stanley, Nat. Photonics 2012, 6, 146.
- [4] J. J. Krich, B. I. Halperin, A. Aspuru-Guzik, J. Appl. Phys. 2012, 112, 13707.
- [5] M.-J. Sher, C. B. Simmons, J. J. Krich, A. J. Akey, M. T. Winkler, D. Recht, T. Buonassisi, M. J. Aziz, A. M. Lindenberg, Appl. Phys. Lett. 2014, 105, 53905
- [6] R. S. Quimby, Photonics and Lasers, Wiley-Interscience, Hoboken, NJ 2006.
- [7] J. Sickel, A. Ahrens, A. L. Baumann, W. Schade, S. Kontermann, M. Seibt, Phys. Status Solidi A 2017, 214, 1700264.
- [8] Z. Sun, M. C. Gupta, J. Appl. Phys. 2018, 124, 223103.
- [9] M. J. Smith, Y.-T. Lin, M.-J. Sher, M. T. Winkler, E. Mazur, S. Gradečak, J. Appl. Phys. 2011, 110, 053524.
- [10] M. J. Smith, M.-J. Sher, B. Franta, Y.-T. Lin, E. Mazur, S. Gradečak, J. Appl. Phys. 2012, 112, 083518.
- [11] P. Saring, A. Lena Baumann, B. Schlieper-Ludewig, S. Kontermann, W. Schade, M. Seibt, Appl. Phys. Lett. 2013, 103, 061904.
- [12] W. Shockley, W. T. Read, Phys. Rev. 1952, 87, 835.
- [13] R. N. Hall, Phys. Rev. 1952, 87, 387.
- [14] M. A. Green, Solar Cells: Operating Principles, Technology, and System Applications, Prentice-Hall, Inc., Englewood Cliffs, NJ 1982.
- [15] D. Recht, D. Hutchinson, T. Cruson, A. DiFranzo, A. McAllister, A. J. Said, J. M. Warrender, P. D. Persans, M. J. Aziz, Appl. Phys. Express 2012, 5, 41301.
- [16] E. Antolín, A. Martí, J. Olea, D. Pastor, G. González-Díaz, I. Mártil, A. Luque, Appl. Phys. Lett. 2009, 94, 42115.
- [17] M. Otto, M. Algasinger, H. Branz, B. Gesemann, T. Gimpel, K. Füchsel, T. Käsebier, S. Kontermann, S. Koynov, X. Li,

- V. Naumann, J. Oh, A. N. Sprafke, J. Ziegler, M. Zilk, R. B. Wehrspohn, *Adv. Opt. Mater.* **2015**, *3*, 147.
- [18] P. D. Persans, N. E. Berry, D. Recht, D. Hutchinson, H. Peterson, J. Clark, S. Charnvanichborikarn, J. S. Williams, A. DiFranzo, M. J. Aziz, J. M. Warrender, Appl. Phys. Lett. 2012, 101, 111105.
- [19] R. A. Sinton, A. Cuevas, Appl. Phys. Lett. 1996, 69, 2510.
- [20] X. Liu, B. Radfar, K. Chen, E. Palikko, T. P. Pasanen, V. Vahanissi, H. Savin. IEEE Photonics Technol. Lett. 2022, 34, 870.
- [21] C. H. Crouch, J. E. Carey, M. Shen, E. Mazur, F. Y. Gnin, Appl. Phys. A 2004, 79, 1635.
- [22] J. Giner Martínez-Sierra, O. Galilea San Blas, J. M. Marchante Gayón, J. I. García Alonso, Spectrochim. Acta, Part B 2015, 108, 35.
- [23] D. E. Kane, R. M. Swanson, in *Proceedings of the 18th IEEE Photovoltaic Specialists Conference* **1985**, pp. 578.
- [24] D. A. Clugston, P. A. Basore, in Proceedings of th 26th IEEE Photovoltaic Specialists Conference 1997, pp. 207–210.
- [25] J. S. Swirhun, R. A. Sinton, M. K. Forsyth, T. Mankad, Prog. Photovoltaics 2011, 19, 313.
- [26] S. Schäfer, P. McKearney, S. Paulus, S. Kontermann, J. Appl. Phys. 2022, 131, 243102.
- [27] E. D. Palik, Handbook of Optical Constants of Solids, Academic Press, San Diego, CA 2003.
- [28] X. G. Zhang, Electrochemistry of Silicon and Its Oxide, Kluwer Academic Publishers, New York, NY 2004.
- [29] S. Paulus, M. Roser, P. McKearney, M. Will, S. Schäfer, S. Kontermann, Semicond. Sci. Technol. 2023, 38, 24002.
- [30] L. Frey, C. Lehrer, H. Ryssel, Appl. Phys. A 2003, 76, 1017.
- [31] N. Gosset, M. Boufnichel, E. Bahette, W. Khalfaoui, R. Ljazouli, V. Grimal-Perrigouas, R. Dussart, J. Micromech. Microeng. 2015, 25, 95011.
- [32] C. H. Wang, K. Misiakos, A. Neugroschel, *IEEE Trans. Electron Devices* **1990**, *37*, 1314.
- [33] M. S. Tyagi, R. van Overstraeten, Solid-State Electron. 1983, 26, 577.
- [34] M. T. Winkler, M.-J. Sher, Y.-T. Lin, M. J. Smith, H. Zhang, S. Gradečak, E. Mazur, J. Appl. Phys. 2012, 111, 093511.
- [35] M.-J. Sher, E. Mazur, Appl. Phys. Lett. 2014, 105, 032103.
- [36] M. Tabbal, T. Kim, J. M. Warrender, M. J. Aziz, B. L. Cardozo, R. S. Goldman, J. Vac. Sci. Technol., B: Microelectron. Nanometer Struct. –Process., Meas., Phenom. 2007, 25, 1847.
- [37] C.-H. Li, J.-H. Zhao, Q.-D. Chen, J. Feng, W.-T. Zheng, H.-B. Sun, IEEE Photonics Technol. Lett. 2015, 27, 1481.
- [38] R. Younkin, J. E. Carey, E. Mazur, J. A. Levinson, C. M. Friend, J. Appl. Phys. 2003, 93, 2626.
- [39] C. Wu, C. H. Crouch, L. Zhao, E. Mazur, Appl. Phys. Lett. 2002, 81, 1999.
- [40] W. B. Jackson, N. M. Johnson, D. K. Biegelsen, Appl. Phys. Lett. 1983, 43, 195.
- [41] C.-H. Li, X.-P. Wang, J.-H. Zhao, D.-Z. Zhang, X.-Y. Yu, X.-B. Li, J. Feng, Q.-D. Chen, S.-P. Ruan, H.-B. Sun, *IEEE Sens. J.* 2018, 18, 3595
- [42] X. Dong, N. Li, Z. Zhu, H. Shao, X. Rong, C. Liang, H. Sun, G. Feng, L. Zhao, J. Zhuang, Appl. Phys. Lett. 2014, 104, 091907.
- [43] K. Wang, H. Yang, X. Wang, Y. Wang, Z. Li, J. Gao, B. Li, J. Gao, Appl. Phys. Express 2018, 11, 62203.
- [44] P. Mc Kearney, S. Schäfer, S. Paulus, M. Roser, F. Piermaier, I. Lebershausen, S. R. Kontermann, J. Appl. Phys. 2023, 133, 13102.
- [45] X. Liu, B. Radfar, K. Chen, O. E. Setala, T. P. Pasanen, M. Yli-Koski, H. Savin, V. Vahanissi, *IEEE Trans. Semicond. Manuf.* 2022, 35, 504.